Communication

Nano Research
2023, 16(4): 4874–4879

ISSN 1998-0124 CN 11-5974/O4
https://doi.org/10.1007/s12274-022-5154-0

Biomass-derived hard carbon microtubes with tunable apertures for high-performance sodium-ion batteries

Pin Song[1,2,3,§] (✉), Shiqiang Wei[4,§], Jun Di[5], Jun Du[1], Wenjie Xu[4], Daobin Liu[4], Changda Wang[4], Sicong Qiao[4], Yuyang Cao[4], Qilong Cui[4], Pengjun Zhang[4], Liaobo Ma[6], Jiewu Cui[3], Yan Wang[3], and Yujie Xiong[1,4] (✉)

[1] *Key Laboratory of Functional Molecular Solids, Ministry of Education, Anhui Engineering Research Center of Carbon Neutrality, Anhui Laboratory of Molecule-Based Materials, College of Chemistry and Materials Science, Anhui Normal University, Wuhu 241000, China*
[2] *Key Laboratory of Advanced Energy Materials Chemistry (Ministry of Education), College of Chemistry, Nankai University, Tianjin 300071, China*
[3] *Key Laboratory of Advanced Functional Materials and Devices of Anhui Province, Hefei University of Technology, Hefei 230009, China*
[4] *National Synchrotron Radiation Laboratory, Chinese Academy of Sciences (CAS) Center for Excellence in Nanoscience, School of Chemistry and Materials Science, University of Science and Technology of China, Hefei 230029, China*
[5] *School of Chemistry and Chemical Engineering, National Special Superfine Powder Engineering Research Center, Nanjing University of Science and Technology, Nanjing 210094, China*
[6] *School of Materials Science and Engineering, Anhui University of Technology, Maanshan 243002, China*
[§] *Pin Song and Shiqiang Wei contributed equally to this work.*

Received: 10 August 2022 / **Revised:** 22 September 2022 / **Accepted:** 6 October 2022

ABSTRACT

Sodium-ion batteries (SIBs) are considered the most up-and-coming complements for large-scale energy storage devices due to the abundance and cheap sodium. However, due to the bigger radius, it is still a great challenge to develop anode materials with suitable space for the intercalation of sodium ions. Herein, we present hard carbon microtubes (HCTs) with tunable apertures derived from low-cost natural kapok fibers via a carbonization process for SIBs. The resulted HCTs feature with smaller surface area and shorter Na^+ diffusion path benefitting from their unique micro-nano structure. Most importantly, the wall thickness of HCTs could be regulated and controlled by the carbonization temperature. At a high temperature of 1,600 °C, the carbonized HCTs possess the smallest wall thickness, which reduces the diffusion barrier of Na^+ and enhances the reversibility Na^+ storage. As a result, the 1600HCTs deliver a high initial Coulombic efficiency of 90%, good cycling stability (89.4% of capacity retention over 100 cycles at 100 $mA \cdot g^{-1}$), and excellent rate capacity. This work not only charts a new path for preparing hard carbon materials with adequate ion channels and novel tubular micro-nano structures but also unravels the mechanism of hard carbon materials for sodium storage.

KEYWORDS

hard carbon, kapok fibers, sodium-ion batteries (SIBs), reversible capacity, long cycle life

1 Introduction

Developing energy storage technology is one of the key technologies to realizing the efficient utilization of renewable energy, since the massive green-house gas emissions have become a global challenge. Sodium-ion batteries (SIBs) have been credited as a promising alternative for large-scale applications owing to the abundance and cheapness of sodium resources. However, due to the bigger radius of sodium, conventional graphite is not applicable to SIBs. Therefore, the development of anode materials with low-cost and high-performance features has been a key step for the improved performance of SIBs [1–7]. The research of anode materials mainly focuses on carbon materials, oxides, sulfides, phosphides, organic compounds, and alloy materials [8–23], including graphene sheets, hard carbon, SnO_2, MoS_2, NiP_3, $NaxCoO_2$, $Na_2C_8H_4O_4$, and Si-Sb alloy [24–31]. Among them, hard carbon with randomly oriented graphitic layers has been widely implemented as the most promising anode material [32]. Nevertheless, it is still confronted with low reversible capacity and initial coulombic efficiency in the early works [33–36]. Recent studies have significantly improved the reversible ability and cyclic stability of this kind of material [37–40]. However, there are still some problems, such as poor cyclic stability and inferior rate performance, which impede its industrialization application in practical SIBs. Nano-sized hard carbons have good electrochemical properties on account of the sufficient contact between the electrolyte and electrode interface and short diffusion path of Na^+ ion [41, 42]. However, serious side reactions could be occurred as a result of the large surface area, leading to a low Coulombic efficiency. Meanwhile, the micro-sized hard carbon material with a low surface area tends to increase high initial Coulombic efficiency, but the cycle stability and rate performance are poor due to the longer diffusion path of Na^+ ion [8]. To combine the advantages of nano- and micro-scale materials, an effective strategy of the micro-nano structure was proposed [43, 44].

Address correspondence to Pin Song, songpin@ahnu.edu.cn; Yujie Xiong, yjxiong@ustc.edu.cn

清華大學出版社 Tsinghua University Press Springer

Herein, we demonstrate to use renewable biomass of kapok fibers as a precursor for preparing hard carbon with a micro-nano structure by a pyrolysis method at 1,200 °C (1200HCTs), 1,400 °C (1400HCTs), and 1,600 °C (1600HCTs), which have been suggested as the most suitable carbonizing temperatures [9, 45–48]. The results show that the carbonized products have a great enhancement in initial Coulombic efficiency, reversible capacity, and excellent rate capability. Most importantly, the as-prepared HCTs exhibit tunable apertures, which provides a good opportunity to obtain sufficient passageways for Na^+ shuttle.

2 Results and discussion

To elucidate the microstructure of the hard carbon materials, X-ray diffraction (XRD) was employed (Fig. 1(a)). All XRD patterns show two broad diffraction peaks at 24° and 43°. The peak centered at $2\theta \approx 24°$ is observed for all samples which correspond to (002) planes of expanded graphite [49]. The peak patterns of HCTs had no obvious change with the increase of carbonization temperature, indicating the nature of hard carbon. The (002) peak position shifts to a higher angle with increasing heat-treatment temperature, indicating the local structural development to a short-range ordering and the decrease of d_{002} (Table S1 in the Electronic Supplementary Material (ESM)).

The kapok fibers have a diameter of 15 to 30 μm and a wall thickness of 0.9–1 μm (Fig. S1 in the ESM). During the pyrolysis process, kapok fibers undergo aromatization and polycondensation reactions and eventually form short graphite layers. The morphology of the carbonized kapok fiber has remained where the diameter and the wall thickness from scanning electron microscopy (SEM) images are 5–10 μm and 100–300 nm, respectively (Fig. 1(b) and Fig. S2 in the ESM). The wall thickness decreases gradually with the increase of carbonization temperature. At carbon temperatures of 1,200, 1,400, and 1,600 °C, the wall thickness is 243, 200, and 187 nm, respectively (Figs. 1(d)–1(f)). Compared with bulk counterparts, the micron tube structure is able to facilitate the diffusion of liquid electrolyte while the nanostructure can shorten the solid-state diffusion length of Na^+. As shown in high-resolution transmission electron microscopy (HRTEM) and the inserted selected area electron diffraction (SAED) pattern (Fig. S3 in the ESM), the 1600HCTs display non-graphitized structure. A diffraction ring is observed in the SAED pattern. The specific surface area and pore size of three HCTs are detected by the nitrogen adsorption/desorption method (Fig. 1(c) and Fig. S4 in the ESM). The specific surface area of the HCTs gradually decreases with increasing carbonization temperature (Fig. S4 in the ESM). It should better reduce the solid electrolyte interface (SEI) formation and improve the initial Coulombic efficiency [46]. In addition, the pore size increases with the increase in carbonization temperature (Fig. 1(c)), which is mainly caused by the thinning of pore wall with the increased temperature.

The thermogravimetric analysis (TGA) curves are shown in Fig. S5 in the ESM. From 20 to 124 °C, the weight of the kapok fiber decreases slightly (~ 15%), which is mainly due to the evaporation of water. Then, the weight dropped sharply (~ 83%) from 124 to 528 °C, indicating that the main reaction occurred at this stage. Finally, it remains the ~ 10% weight of the original material and has no change as the temperature increases to ~ 1,200 °C, suggesting that there are not any more chemical reactions in this region. The TGA result shows that the carbonization mainly occurs in the temperature ranges of 124–528 °C. It has demonstrated that the high temperature is beneficial to obtain the porous carbon structure with high specific area [50, 51]. Figure S6 in the ESM shows the Raman spectra of samples and all the carbonized samples exhibit two peaks corresponding to the D band at 1,327 cm^{-1} and G band at 1,587 cm^{-1}. The relative intensity ratios (I_D/I_G) increase with carbonization temperature [51, 52]. The I_D/I_G value increased from 1.03 to 1.1 (Fig. S6(b) and Table S1 in the ESM), indicating that the structural defects of hard carbon micro-nano tubes increased due to the increase in carbonization temperature [53]. Figure S7 and Table S2 in the ESM show the energy dispersive X-ray spectroscopy (EDS) results of the element species and distribution of 1600HCTs. Compared with other biomass-derived carbons, the HCTs have high carbon purity.

The X-ray photoelectron spectroscopy (XPS) spectra of the kapok fiber and the derived HCTs are shown in Figs. 2(a)–2(e). These materials are composed of the C and O elements (Fig. 2(a)). The C 1s peaks are deconvoluted into two peaks belonging to C=C/C–C (284.71 eV) and C–O (286.17 eV) groups [54]. With the increase of carbonization temperature, XPS results indicate the component of C–O bonds decreases while the component of C=C/C–C bonds increases (Figs. 2(b)–2(e)). Figure 2(f) shows the C K-edge near-edge X-ray absorption fine structure (NEXAFS) spectral region for the kapok fiber derived HCTs with thermal activation at 1,200, 1,400, and 1,600 °C, respectively. The C K-edge spectrum measured at 1,200 °C shows the features at 285.9, 288.1, 289.2, 291.1, 292.2, and 293.4 eV. As increasing the temperature of thermal treatment, all features in the spectrum increase in

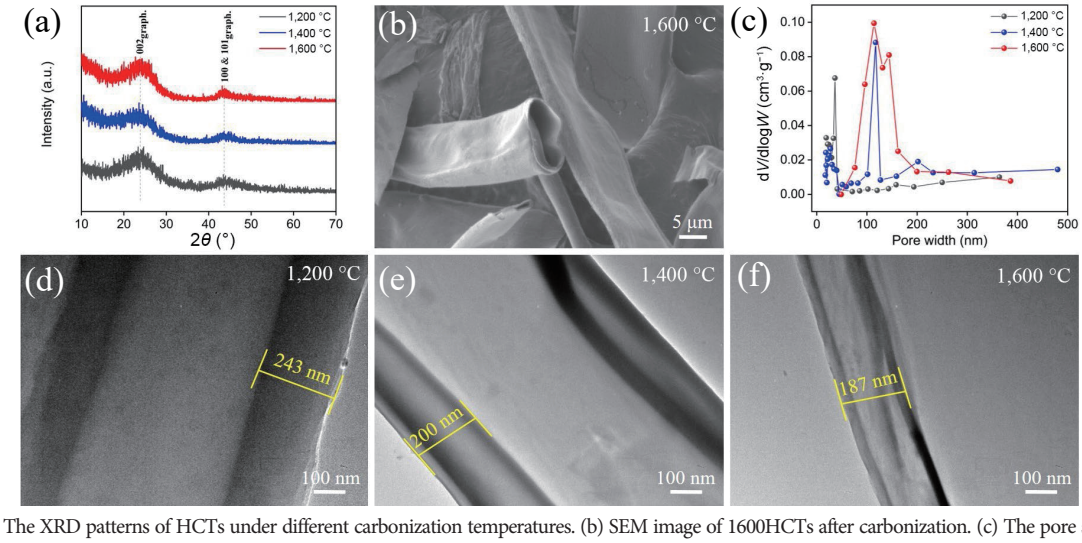

Figure 1 (a) The XRD patterns of HCTs under different carbonization temperatures. (b) SEM image of 1600HCTs after carbonization. (c) The pore size distribution under different carbonization temperatures. TEM images of (d) 1200HCTs, (e) 1400HCTs, and (f) 1600HCTs after carbonization.

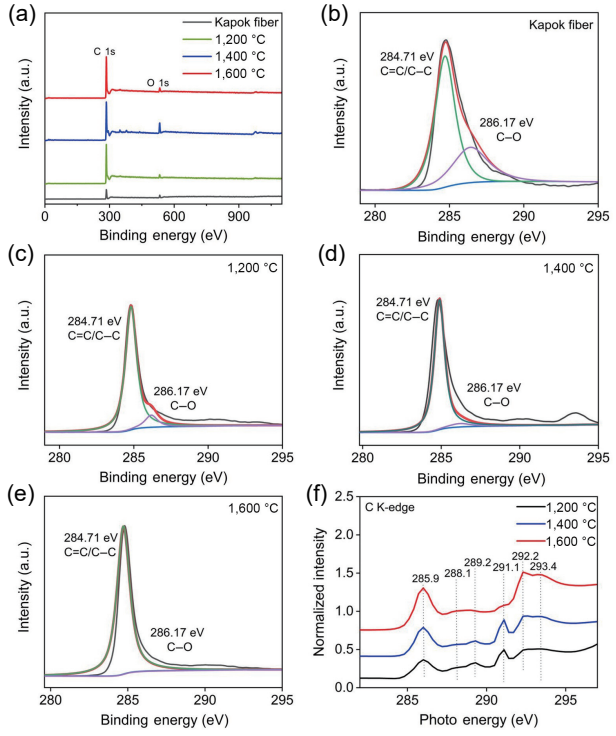

Figure 2 (a)–(e) The XPS survey spectra related C 1s spectra for the kapok fiber and the kapok fiber carbonized at different temperatures. (f) C K-edge NEXAFS of kapok fiber after heating to 1,200, 1,400, and 1,600 °C.

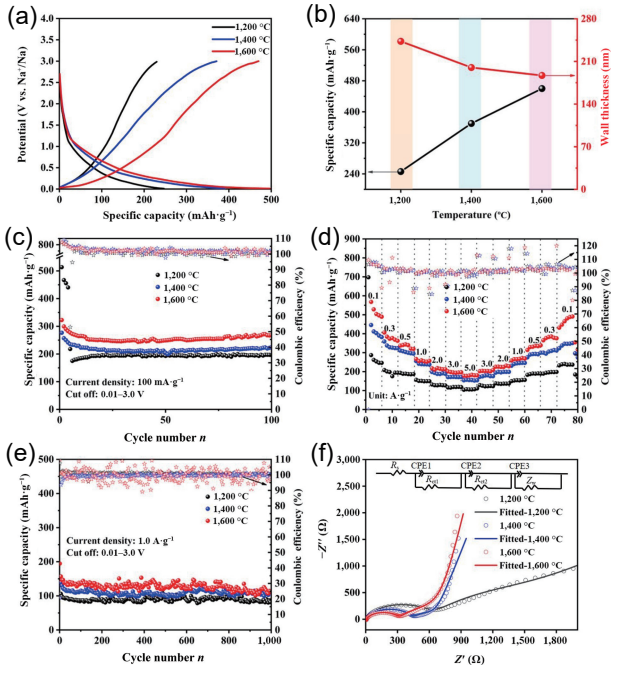

Figure 3 (a) Galvanostatic charge–discharge profiles of HCTs at 100 mA·g^{-1}. (b) Graph of carbonization temperature versus reversible capacity and wall thickness. (c) Cyclic performance of HCTs at 100 mA·g^{-1}. (d) Rate capability of HCTs at various currents. (e) Cyclic performance of HCTs at 1 A·g^{-1}. (f) Nyquist plots and fitted plots of HCTs electrodes.

intensity except for those at 288.1, 289.2, and 291.1 eV, where the intensity significantly decreases. The shoulder at 288.1 eV disappears after the heat treatment at 1,400 °C. The features at 289.2 and 291.1 eV gradually decrease in the range 1,400–1,600 °C. The features at 288.1, 289.2, and 291.1 eV are ascribed to oxygenated functionalities on the nanotubes and these functionalities decompose upon the heat treatment [55, 56]. That the features at 285.9 and 292.2 eV increase in intensity can be attributed to the increase of overall crystallinity and the decrease of defects at the elevated temperature.

The electrochemical performance of prepared samples assembled in half coin cells was evaluated by galvanostatic discharge–charge experiments. The electrochemical performance of 1600HCTs was carried out in different electrolytes as shown in Fig. S8 in the ESM. The electrode in the $NaClO_4$ electrolyte shows a higher initial Coulombic efficiency and reversible capacity, compared to those in the $NaPF_6$ electrolyte. Therefore, we choose $NaClO_4$ electrolyte for further electrochemical tests. As shown in Fig. 3(a), these HCTs samples exhibited a similar sodium storage behavior attributed to the low specific surface areas [32, 46]. The charge–discharge profiles exhibit two distinct parts: slope areas above 0.1 V and a plateau region around 0–0.1 V, indicating two different sodium storage mechanisms, which is also verified by the cyclic voltammetry (CV) results (Fig. S9 in the ESM). It can be seen from TEM images (Figs. 1(d)–1(f)) that the wall thickness decreases with the increase of carbonization temperature, and the pore size increase, which is conducive to the increased reversible capacity due to the fast ion migration in bigger pore (Fig. 3(b)). As can be seen from Fig. 3(c), these carbonization samples show a high initial Coulombic efficiency of around 80% as a result of the low specific surface areas [32]. The reversible capacity of 1600HCTs is 299.7 mAh·g^{-1} at 0.1 A·g^{-1}, much better than those of the 1400HCTs (257 mAh·g^{-1}) and 1200HCTs (217.9 mAh·g^{-1}). The 1600HCTs have a higher capacity, which may be caused by the lower specific surface area and more closing pores obtained at the high pyrolysis temperature [57]. Due to the unique hollow micro-nano structure, the electrolyte infiltration is better and the diffusion distance of sodium ion is shorter, and the HCTs possess excellent rate capability (Fig. 3(d)). The 1600HCTs deliver a superior rate performance with respect to specific capacities of 358, 272, and 213 mAh·g^{-1} at current rates of 0.5, 1, and 2 A·g^{-1}, respectively. Compared with previously reported hard carbon materials, 1600HCTs showed excellent sodium storage, cycling stability, and capacity retention ratio (Table S3 and Fig. S10 in the ESM). 1600HCTs as the biomass-based hard carbon materials exhibit good capacity retention at the anode of SIBs. Figure 3(e) shows the cycling performance of HCTs. After 1,000 cycles, the reversible specific capacity of the 1600HCTs is 109 mAh·g^{-1} at the current density of 1 A·g^{-1}, which is attributed to the stable micro-nano structure. After long-term cycling, the structure of 1600HCTs does not change significantly (Fig. S11 in the ESM), indicating the stability of micro-nano structure. Figure 3(f) shows the Nyquist plots of the 1200HCTs, 1400HCTs, and 1600HCTs electrodes that performed 200 charge–discharge cycles at 100 mA·g^{-1}. Both Nyquist plots consist of two regions, which are sloping lines at the low-frequencies and semicircles at the high-frequencies. The charge-transfer resistance (412 Ω) of the 1600HCTs electrode is lower than those of the 1400HCTs (430 Ω) and 1200HCTs (580 Ω) electrodes (Fig. 3(f)), indicating that the high carbonization temperature can significantly improve charge transfer in the electrochemical reaction, and thus achieve excellent sodium storage, cycle stability, and rate performance.

To further reveal the relationship between the samples carbonized at different temperatures and the corresponding rate capabilities, we have employed galvanostatic intermittent titration technique (GITT) to calculate the apparent diffusion coefficient of Na ions in HCTs electrodes by charge/discharge for 1 min time and standing for 30 min at a constant current of 100 mA·g^{-1} (Fig. 4 and Fig. S12 in the ESM). In the whole process of charge and discharge, the program is repeatedly applied to the battery. According to GITT results, the diffusion coefficient of Na^+ (D_{Na^+}, cm^2·s^{-1}) was calculated based on the following equation

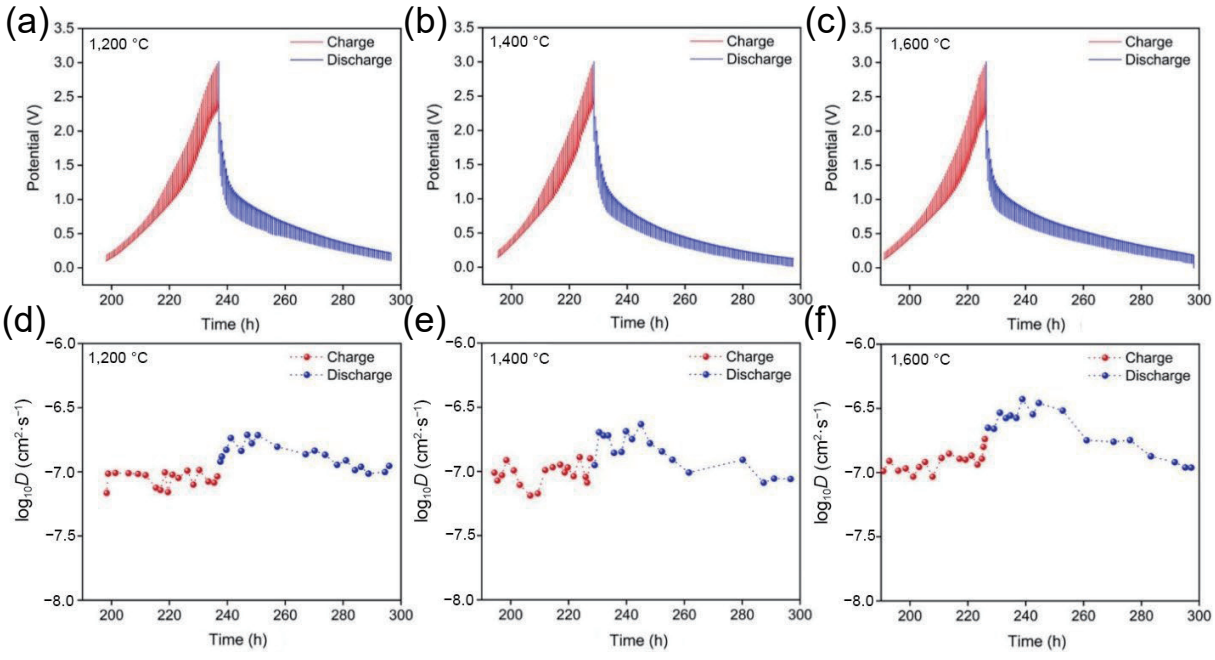

Figure 4 GITT curves and calculation of corresponding Na^+ diffusion coefficient of Na||HCTs cell.

$$D_{Na^+} = \frac{4}{\pi\tau}\left(\frac{m_B V_M}{M_B S}\right)^2\left(\frac{\Delta E_S}{\Delta E_\tau}\right)^2$$

where τ represents the duration of the current pulse, m_B corresponds to the mass of the active material, M_B and V_M are related to the molar mass and molar volume, and S is the active surface area of the HCT electrodes. ΔE_S is the open-circuit voltage difference measured at the end of two successive relaxation cycles, and ΔE_τ is the voltage change (V) during the constant current pulse. Both of ΔE_S and ΔE_τ can be obtained from the GITT curves (Fig. S12 in the ESM). As shown in Figs. 4(d)–4(f), the Na ions diffusivity coefficients of all three samples are between 10^{-7} and 10^{-6} $cm^2 \cdot s^{-1}$. For the 1600HCTs, the diffusivity coefficient is great than those of 1400HCTs and 1200HCTs, indicating the superior ion diffusion which ensures the high-rate performance of 1600HCTs when used as anode materials for SIBs.

3 Conclusions

In conclusion, we use renewable kapok fibers as precursors to fabricate hard carbon materials with tunable apertures and micro-nano structure via one-step pyrolysis. The as-prepared 1600HCTs as the anode of SIBs have a superior electrochemical performance with large initial Coulombic efficiency, high reversible capacity, and good rate performance. The micro structured hard carbon material with a low surface area is responsible for the high initial Coulombic efficiency. On the other hand, the nano-sized tube wall can enhance the electrolyte infiltration and shorten the diffusion distance of Na ions. The unique hierarchical micro-nano structure improves the sodium storage and rate performance of the 1600HCTs. These results provide a facile strategy for preparing hard carbons from biomass materials and guidance for the improved performance of the anode of SIBs by regulating the pore structure of carbon materials.

4 Experimental section

4.1 Preparation of the hard carbon micro-nano tube

Kapok fibers were washed several times by deionized water, and vacuum dried at 80 °C for 24 h. Then the dried kapok fiber was transferred to a tube furnace for pyrolysis under Ar gas atmosphere. After that, the furnace was heated from 25 to 1200, 1400, and 1600 °C at a rate of 5 °C·min^{-1} and kept at 1200, 1400, and 1600 °C for 4 h, respectively. Finally, after cooling naturally, the corresponding obtained samples were marked as 1200HCTs, 1400HCTs, and 1600HCTs.

4.2 Characterization

The morphology of samples was obtained by SEM (Hitachi S-4800, Japan) and TEM (JEOL-JEM-2100Plus, Japan). The structure was characterized by XRD with Cu-Kα radiation (λ = 1.54178 Å) and Raman spectra. The XPS spectra were performed by PHI-5400. The TGA was measured from 25 to 1,200 °C in N_2 gas atmosphere at a rate of 10 °C·min^{-1}. The nitrogen adsorption and desorption isotherms were characterized by ASAP 2020 instrument. The C K-edge was measured at the beamline BL12B of the Hefei Synchrotron Radiation Equipment.

4.3 Electrochemical measurements

All the electrochemical tests were evaluated with half cells. The working electrode was prepared by mixing with active material, acetylene black, and polyvinylidene fluoride (weight ratio 7:2:1) onto copper foil. It was pre-dried in a 70 °C oven and then vacuum dried at 100 °C for 24 h. The loading active material of the electrode was ~ 1 mg·cm^{-2}. Sodium metal was used as the counter electrode. The electrolyte was a solution of 1 M $NaClO_4$ in ethylene carbonate/dimethyl carbonate (1:1 in volume). Glass fibers were used as the separator. All batteries were assembled in an argon-filled glovebox where the water and oxygen content were less than 0.1 ppm. The discharge/charge and CV tests were characterized by an electrochemical workstation in a voltage range of 0.01–3 V. The electrochemical impedance spectra were carried out by frequency range of 0.1–105 Hz at 25 °C. The GITT curves were charged and discharged for 1 min at a specific current of 100 mA·g^{-1}, then relaxed for 30 min to reach the quasi-equilibrium potential.

Acknowledgements

This work was financially supported by the Natural Science Research Project for Universities in Anhui Province (No. KJ2021ZD0006), the Natural Science Foundation of Anhui

Province (No. 2208085MB21), the Fundamental Research Funds for the Central Universities of China (No. PA2022GDSK0056), the University Synergy Innovation Program of Anhui Province (Nos. GXXT-2020-073 and GXXT-2020-074), the National Key R&D Program of China (No. 2020YFA0406103), the National Natural Science Foundation of China (Nos. 21725102, 91961106, 91963108, and 22175165), and Singapore National Research Foundation under NRF RF Award No. Tier 1 2017-T1-001-075. We are very grateful to Professor Zheng Liu form Nanyang Technological University for his support.

Electronic Supplementary Material: Supplementary material (additional SEM images, HRTEM images, adsorption–desorption curves, TGA curve, CV curves, Raman spectra, and other data) is available in the online version of this article at https://doi.org/10.1007/s12274-022-5154-0.

References

[1] Yabuuchi, N.; Kubota, K.; Dahbi, M.; Komaba, S. Research development on sodium-ion batteries. *Chem. Rev.* **2014**, *114*, 11636–11682.

[2] Guo, Y.; Wu, S. C.; He, Y. B.; Kang, F. Y.; Chen, L. Q.; Li, H.; Yang, Q. H. Solid-state lithium batteries: Safety and prospects. *eScience* **2022**, *2*, 138–163.

[3] Zhu, Y. F.; Xiao, Y.; Dou, S. X.; Kang, Y. M.; Chou, S. L. Spinel/post-spinel engineering on layered oxide cathodes for sodium-ion batteries. *eScience* **2021**, *1*, 13–27.

[4] Li, Q.; Liu, X. S.; Tao, Y.; Huang, J. X.; Zhang, J.; Yang, C. P.; Zhang, Y. B.; Zhang, S. W.; Jia, Y. R.; Lin, Q. W. et al. Sieving carbons promise practical anodes with extensible low-potential plateaus for sodium batteries. *Natl. Sci. Rev.* **2022**, *9*, nwac084.

[5] Wang, K. F.; Sun, F.; Wang, H.; Wu, D. Y.; Chao, Y. X.; Gao, J. H.; Zhao, G. B. Altering thermal transformation pathway to create closed pores in coal-derived hard carbon and boosting of Na^+ plateau storage for high-performance sodium-ion battery and sodium-ion capacitor. *Adv. Funct. Mater.* **2022**, *32*, 2203725.

[6] Gu, Z. Y.; Guo, J. Z.; Cao, J. M.; Wang, X. T.; Zhao, X. X.; Zheng, X. Y.; Li, W. H.; Sun, Z. H.; Liang, H. J.; Wu, X. L. An advanced high-entropy fluorophosphate cathode for sodium-ion batteries with increased working voltage and energy density. *Adv. Mater.* **2022**, *34*, 2110108.

[7] Peng, J.; Zhang, W.; Liu, Q. N.; Wang, J. Z.; Chou, S. L.; Liu, H. K.; Dou, S. X. Prussian blue analogues for sodium-ion batteries: Past, present, and future. *Adv. Mater.* **2022**, *34*, 2108384.

[8] Zhu, Y. Y.; Chen, M. M.; Li, Q.; Yuan, C.; Wang, C. Y. High-yield humic acid-based hard carbons as promising anode materials for sodium-ion batteries. *Carbon* **2017**, *123*, 727–734.

[9] Xie, F.; Xu, Z.; Jensen, A. C. S.; Au, H.; Lu, Y. X.; Araullo-Peters, V.; Drew, A. J.; Hu, Y. S.; Titirici, M. M. Hard-soft carbon composite anodes with synergistic sodium storage performance. *Adv. Funct. Mater.* **2019**, *29*, 1901072.

[10] Song, P.; Di, J.; Kang, L. X.; Xu, M. Z.; Tang, B. J.; Xiong, J.; Cui, J. W.; Zeng, Q. S.; Zhou, J. D.; He, Y. M. et al. Enhancing the cycling stability of Na-ion batteries by bonding MoS_2 on assembled carbon-based materials. *Nano Mater. Sci.* **2019**, *1*, 310–317.

[11] Hou, H. S.; Qiu, X. Q.; Wei, W. F.; Zhang, Y.; Ji, X. B. Carbon anode materials for advanced sodium-ion batteries. *Adv. Energy Mater.* **2017**, *7*, 1602898.

[12] Chen, W. M.; Wan, M.; Liu, Q.; Xiong, X. Q.; Yu, F. Q.; Huang, Y. H. Heteroatom-doped carbon materials: Synthesis, mechanism, and application for sodium-ion batteries. *Small Methods* **2019**, *3*, 1800323.

[13] Wang, X. L.; Li, G.; Hassan, F. M.; Li, J. D.; Fan, X. Y.; Batmaz, R.; Xiao, X. C.; Chen, Z. W. Sulfur covalently bonded graphene with large capacity and high rate for high-performance sodium-ion batteries anodes. *Nano Energy* **2015**, *15*, 746–754.

[14] Wang, E. H.; Chen, M. Z.; Guo, X. D.; Chou, S. L.; Zhong, B. H.; Dou, S. X. Synthesis strategies and structural design of porous carbon-incorporated anodes for sodium-ion batteries. *Small Methods* **2020**, *4*, 1900163.

[15] Kumaresan, T. K.; Masilamani, S. A.; Raman, K.; Karazhanov, S. Z.; Subashchandrabose, R. High performance sodium-ion battery anode using biomass derived hard carbon with engineered defective sites. *Electrochim. Acta* **2021**, *368*, 137574.

[16] Yu, K. H.; Wang, X. R.; Yang, H. Y.; Bai, Y.; Wu, C. Insight to defects regulation on sugarcane waste-derived hard carbon anode for sodium-ion batteries. *J. Energy Chem.* **2021**, *55*, 499–508.

[17] Pan, H. L.; Lu, X.; Yu, X. Q.; Hu, Y. S.; Li, H.; Yang, X. Q.; Chen, L. Q. Sodium storage and transport properties in layered $Na_2Ti_3O_7$ for room-temperature sodium-ion batteries. *Adv. Energy Mater.* **2013**, *3*, 1186–1194.

[18] Sun, Y.; Zhao, L.; Pan, H. L.; Lu, X.; Gu, L.; Hu, Y. S.; Li, H.; Armand, M.; Ikuhara, Y.; Chen, L. Q. et al. Direct atomic-scale confirmation of three-phase storage mechanism in $Li_4Ti_5O_{12}$ anodes for room-temperature sodium-ion batteries. *Nat. Commun.* **2013**, *4*, 1870.

[19] Zhao, L.; Zhao, J. M.; Hu, Y. S.; Li, H.; Zhou, Z. B.; Armand, M.; Chen, L. Q. Disodium terephthalate ($Na_2C_8H_4O_4$) as high performance anode material for low-cost room-temperature sodium-ion battery. *Adv. Energy Mater.* **2012**, *2*, 962–965.

[20] Zhang, J. Y.; Li, M.; Kang, Z. W.; Xiao, B. S.; Lin, H. C.; Lu, J. Y.; Liu, H. D.; Zhang, X.; Peng, D. L.; Zhang, Q. B. Atomic mechanisms of hexagonal close-packed Ni nanocrystallization revealed by *in situ* liquid cell transmission electron microscopy. *Nano Res.* **2022**, *15*, 6772–6778.

[21] Cai, M. T.; Zhang, H. H.; Zhang, Y. G.; Xiao, B. S.; Wang, L.; Li, M.; Wu, Y.; Sa, B. S.; Liao, H. G.; Zhang, L. et al. Boosting the potassium-ion storage performance enabled by engineering of hierarchical MoSSe nanosheets modified with carbon on porous carbon sphere. *Sci. Bull.* **2022**, *67*, 933–945.

[22] Li, Y. P.; Zhang, Q. B.; Yuan, Y. F.; Liu, H. D.; Yang, C. H.; Lin, Z.; Lu, J. Surface amorphization of vanadium dioxide (B) for K-ion battery. *Adv. Energy Mater.* **2020**, *10*, 2000717.

[23] Ke, C. Z.; Shao, R. W.; Zhang, Y. G.; Sun, Z. F.; Qi, S.; Zhang, H. H.; Li, M.; Chen, Z. L.; Wang, Y. S.; Sa, B. S. et al. Synergistic engineering of heterointerface and architecture in new-type ZnS/Sn heterostructures *in situ* encapsulated in nitrogen-doped carbon toward high-efficient lithium-ion storage. *Adv. Funct. Mater.* **2022**, *32*, 2205635.

[24] Kalisvaart, W. P.; Olsen, B. C.; Luber, E. J.; Buriak, J. M. Sb-Si alloys and multilayers for sodium-ion battery anodes. *ACS Appl. Energy Mater.* **2019**, *2*, 2205–2213.

[25] Lao, M. M.; Zhang, Y.; Luo, W. B.; Yan, Q. Y.; Sun, W. P.; Dou, S. X. Alloy-based anode materials toward advanced sodium-ion batteries. *Adv. Mater.* **2017**, *29*, 1700622.

[26] Tomboc, G. M.; Wang, Y. T.; Wang, H.; Li, J. H.; Lee, K. Sn-based metal oxides and sulfides anode materials for Na ion battery. *Energy Stor. Mater.* **2021**, *39*, 21–44.

[27] Ying, H. J.; Han, W. Q. Metallic Sn-based anode materials: Application in high-performance lithium-ion and sodium-ion batteries. *Adv. Sci.* **2017**, *4*, 1700298.

[28] Ma, W. S.; Yin, K. B.; Gao, H.; Niu, J. Z.; Peng, Z. Q.; Zhang, Z. H. Alloying boosting superior sodium storage performance in nanoporous tin-antimony alloy anode for sodium ion batteries. *Nano Energy* **2018**, *54*, 349–359.

[29] Yu, X. Q.; Pan, H. L.; Wan, W.; Ma, C.; Bai, J. M.; Meng, Q. P.; Ehrlich, S. N.; Hu, Y. S.; Yang, X. Q. A size-dependent sodium storage mechanism in $Li_4Ti_5O_{12}$ investigated by a novel characterization technique combining *in situ* X-ray diffraction and chemical sodiation. *Nano Lett.* **2013**, *13*, 4721–4727.

[30] Wang, Y. S.; Yu, X. Q.; Xu, S. Y.; Bai, J. M.; Xiao, R. J.; Hu, Y. S.; Li, H.; Yang, X. Q.; Chen, L. Q.; Huang, X. J. A zero-strain layered metal oxide as the negative electrode for long-life sodium-ion batteries. *Nat. Commun.* **2013**, *4*, 2365.

[31] Wu, X. Y.; Ma, J.; Ma, Q. D.; Xu, S. Y.; Hu, Y. S.; Sun, Y.; Li, H.; Chen, L. Q.; Huang, X. J. A spray drying approach for the synthesis of a $Na_2C_6H_2O_4$/CNT nanocomposite anode for sodium-ion batteries. *J. Mater. Chem. A* **2015**, *3*, 13193–13197.

[32] Stevensa, D. A.; Dahn, J. R. High capacity anode materials for rechargeable sodium-ion batteries. *J. Electrochem. Soc.* **2000**, *147*, 1271–1273.
[33] Doeff, M. M.; Ma, Y. P.; Visco, S. J.; De Jonghe, L. C. Electrochemical insertion of sodium into carbon. *J. Electrochem. Soc.* **1993**, *140*, L169–L170.
[34] Izanzar, I.; Dahbi, M.; Kiso, M.; Doubaji, S.; Komaba, S.; Saadoune, I. Hard carbons issued from date palm as efficient anode materials for sodium-ion batteries. *Carbon* **2018**, *137*, 165–173.
[35] Xiao, L. F.; Cao, Y. L.; Henderson, W. A.; Sushko, M. L.; Shao, Y. Y.; Xiao, J.; Wang, W.; Engelhard, M. H.; Nie, Z. M.; Liu, J. Hard carbon nanoparticles as high-capacity, high-stability anodic materials for Na-ion batteries. *Nano Energy* **2016**, *19*, 279–288.
[36] Chen, X. L.; Zheng, Y. H.; Liu, W. J.; Zhang, C.; Li, S.; Li, J. High-performance sodium-ion batteries with a hard carbon anode: Transition from the half-cell to full-cell perspective. *Nanoscale* **2019**, *11*, 22196–22205.
[37] Shen, L. Y.; Shi, S. S.; Roy, S.; Yin, X. P.; Liu, W. B.; Zhao, Y. F. Recent advances and optimization strategies on the electrolytes for hard carbon and P-based sodium-ion batteries. *Adv. Funct. Mater.* **2021**, *31*, 2006066.
[38] Liang, J. L.; Wu, W. W.; Xu, L.; Wu, X. H. Highly stable Na metal anode enabled by a multifunctional hard carbon skeleton. *Carbon* **2021**, *176*, 219–227.
[39] Chen, D. Q.; Zhang, W.; Luo, K. Y.; Song, Y.; Zhong, Y. J.; Liu, Y. X.; Wang, G. K.; Zhong, B. H.; Wu, Z. G.; Guo, X. D. Hard carbon for sodium storage: Mechanism and optimization strategies toward commercialization. *Energy Environ. Sci.* **2021**, *14*, 2244–2262.
[40] Schutjajew, K.; Tichter, T.; Schneider, J.; Antonietti, M.; Roth, C.; Oschatz, M. Insights into the sodiation mechanism of hard carbon-like materials from electrochemical impedance spectroscopy. *Phys. Chem. Chem. Phys.* **2021**, *23*, 11488–11500.
[41] Cao, Y. L.; Xiao, L. F.; Sushko, M. L.; Wang, W.; Schwenzer, B.; Xiao, J.; Nie, Z. M.; Saraf, L. V.; Yang, Z. G.; Liu, J. Sodium ion insertion in hollow carbon nanowires for battery applications. *Nano Lett.* **2012**, *12*, 3783–3787.
[42] Zou, L. L.; Kitta, M.; Hong, J. H.; Suenaga, K.; Tsumori, N.; Liu, Z.; Xu, Q. Fabrication of a spherical superstructure of carbon nanorods. *Adv. Mater.* **2019**, *31*, 1900440.
[43] Qi, J.; Lai, X. Y.; Wang, J. Y.; Tang, H. J.; Ren, H.; Yang, Y.; Jin, Q.; Zhang, L. J.; Yu, R. B.; Ma, G. H. et al. Multi-shelled hollow micro-/nanostructures. *Chem. Soc. Rev.* **2015**, *44*, 6749–6773.
[44] Zhao, L. N.; Zhao, H. L.; Wang, J.; Zhang, Y.; Li, Z. L.; Du, Z. H.; Świerczek, K.; Hou, Y. L. Micro/nano $Na_3V_2(PO_4)_3$/N-doped carbon composites with a hierarchical porous structure for high-rate pouch-type sodium-ion full-cell performance. *ACS Appl. Mater. Interfaces* **2021**, *13*, 8445–8454.
[45] Dou, X. W.; Hasa, I.; Saurel, D.; Vaalma, C.; Wu, L. M.; Buchholz, D.; Bresser, D.; Komaba, S.; Passerini, S. Hard carbons for sodium-ion batteries: Structure, analysis, sustainability, and electrochemistry. *Mater. Today* **2019**, *23*, 87–104.
[46] Yu, Z. E.; Lyu, Y. C.; Wang, Y. T.; Xu, S. Y.; Cheng, H. Y.; Mu, X. Y.; Chu, J. Q.; Chen, R. M.; Liu, Y.; Guo, B. K. Hard carbon micro-nano tubes derived from kapok fiber as anode materials for sodium-ion batteries and the sodium-ion storage mechanism. *Chem. Commun.* **2020**, *56*, 778–781.
[47] Chen, D. Q.; Luo, K. Y.; Yang, Z. W.; Zhong, Y. J.; Wu, Z. G.; Song, Y.; Chen, G.; Wang, G. K.; Zhong, B. H.; Guo, X. D. Direct conversion of ester bond-rich waste plastics into hard carbon for high-performance sodium storage. *Carbon* **2021**, *173*, 253–261.
[48] Ma, Q. L.; Yu, Y. F.; Sindoro, M.; Fane, A. G.; Wang, R.; Zhang, H. Carbon-based functional materials derived from waste for water remediation and energy storage. *Adv. Mater.* **2017**, *29*, 1605361.
[49] Li, Y. M.; Hu, Y. S.; Titirici, M. M.; Chen, L. Q.; Huang, X. J. Hard carbon microtubes made from renewable cotton as high-performance anode material for sodium-ion batteries. *Adv. Energy Mater.* **2016**, *6*, 1600659.
[50] Shultz, J. M.; Walsh, L.; Garfin, D. R.; Wilson, F. E.; Neria, Y. The 2010 Deepwater Horizon oil spill: The trauma signature of an ecological disaster. *J. Behav. Health. Serv. Res.* **2015**, *42*, 58–76.
[51] Song, P.; Cui, J. W.; Di, J.; Liu, D. B.; Xu, M. Z.; Tang, B. J.; Zeng, Q. S.; Xiong, J.; Wang, C. D.; He, Q. et al. Carbon microtube aerogel derived from kapok fiber: An efficient and recyclable sorbent for oils and organic solvents. *ACS Nano* **2020**, *14*, 595–602.
[52] Ding, J.; Wang, H. L.; Li, Z.; Cui, K.; Karpuzov, D.; Tan, X. H.; Kohandehghan, A.; Mitlin, D. Peanut shell hybrid sodium ion capacitor with extreme energy-power rivals lithium ion capacitors. *Energy Environ. Sci.* **2015**, *8*, 941–955.
[53] Park, Y. S.; Choi, Y. C.; Kim, K. S.; Chung, D. C.; Bae, D. J.; An, K. H.; Lim, S. C.; Zhu, X. Y.; Leea, Y. H. High yield purification of multiwalled carbon nanotubes by selective oxidation during thermal annealing. *Carbon* **2001**, *39*, 655–661.
[54] Roldán, L.; Santos, I.; Armenise, S.; Fraile, J. M.; García-Bordejé, E. The formation of a hydrothermal carbon coating on graphite microfiber felts for using as structured acid catalyst. *Carbon* **2012**, *50*, 1363–1372.
[55] Feng, X. F.; Song, M. K.; Stolte, W. C.; Gardenghi, D.; Zhang, D.; Sun, X. H.; Zhu, J. F.; Cairns, E. J.; Guo, J. H. Understanding the degradation mechanism of rechargeable lithium/sulfur cells: A comprehensive study of the sulfur-graphene oxide cathode after discharge–charge cycling. *Phys. Chem. Chem. Phys.* **2014**, *16*, 16931–16940.
[56] Kuznetsova, A.; Popova, I.; Yates, J. T. Jr.; Bronikowski, M. J.; Huffman, C. B.; Liu, J.; Smalley, R. E.; Hwu, H. H.; Chen, J. G. Oxygen-containing functional groups on single-wall carbon nanotubes: NEXAFS and vibrational spectroscopic studies. *J. Am. Chem. Soc.* **2001**, *123*, 10699–10704.
[57] Li, Y. Q.; Lu, Y. X.; Meng, Q. S.; Jensen, A. C. S.; Zhang, Q. Q.; Zhang, Q. H.; Tong, Y. X.; Qi, Y. R.; Gu, L.; Titirici, M. M. et al. Regulating pore structure of hierarchical porous waste cork-derived hard carbon anode for enhanced Na storage performance. *Adv. Energy Mater.* **2019**, *9*, 1902852.